Electronic Supplementary Material (ESI) for Journal of Materials Chemistry A.

Synthesis and Electrochemical Properties of 2D Molybdenum Vanadium Carbides – Solid Solution MXenes

David Pinto[a,b], Babak Anasori[a,b], Hemesh Avireddy[a,b,c], Christopher E. Shuck[a,b], Kanit Hantanasirisakul[a,b], Grayson Deysher[a,b], Joan Ramon Morante[c,d], William Porzio[e], Husam N. Alshareef[f], Yury Gogotsi[a,b]

[a] Department of Materials Science & Engineering, Drexel University, Philadelphia, PA 19104, USA.
[b] A.J. Drexel Nanomaterials Institute, Drexel University, Philadelphia, PA 19104, USA
[c] IREC, Catalonia Institute for Energy Research, Jardins de les Dones de Negre 1, 08930. Sant Adrià de Besòs, Spain
[d] Faculty of Physics, University of Barcelona, Barcelona, Spain
[e] Institute of Chemical Sciences and Technologies "G.Natta" Consiglio Nazionale delle Ricerche (SCI-TEC) via A. Corti 12 20133, Milano, Italy
[f] Materials Science and Engineering, King Abdullah University of Science and Technology (KAUST), Thuwal, 23955-6900, Saudi Arabia

SUPPORTING INFORMATION

Synthesis protocol of Ti_3C_2 MXene films. Ti_3C_2 films were produced by MILD synthesis and vacuum-assisted filtration, as described elsewhere.[1] Briefly, 0.5 g of Ti_3AlC_2 MAX (Carbon-Ukraine) was gradually added (over 30 s) to a stirred etchant solution composed of 10 mL 9 M HCl (Acros Chemicals) and 0.8 g of LiF (Sigma-Aldrich). The mixture was stirred at room temperature for 24 h in a plastic 25 mL container with a loose cap. After etching, the mixture was washed by centrifugation (5 min, 3500 rpm) until the observation of the sediment swelling (pH close to 5). At this step, the centrifugation time is increased to 1 h and the MXene is washed until neutral pH. Finally, the sediment is redispersed and centrifuged at 3500 rpm for 3 min. The supernatant is collected and filtered as a film by vacuum-assisted filtration.

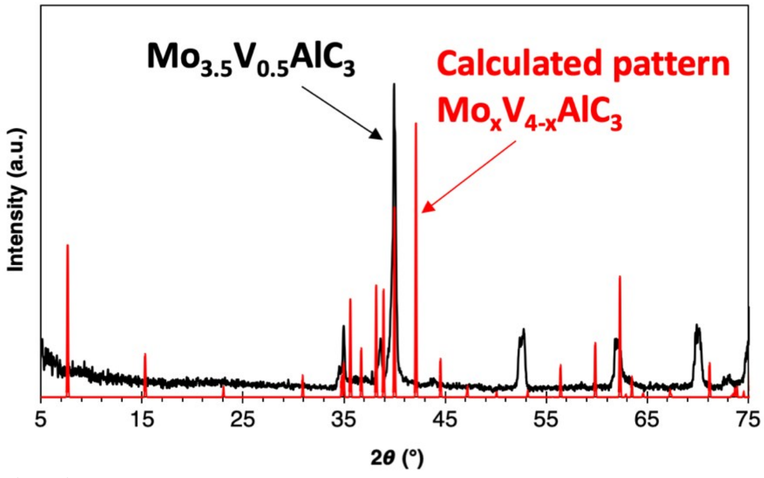

Figure S1. X-ray diffraction (XRD) pattern of high-molybdenum content $Mo_xV_{4-x}AlC_3$ composition, for $x = 3.5$, compared to the expected pattern for $Mo_xV_{4-x}AlC_3$ MAX (hexagonal $P6_3/mmc$ structure). The XRD pattern of $Mo_{3.5}V_{0.5}AlC_3$ composition diverges from the expected $Mo_xV_{4-x}AlC_3$ $P6_3/mmc$ pattern. Most peaks from the expected pattern are absent or significantly shifted and unexpected peaks indicate secondary products and/or unattended structures.

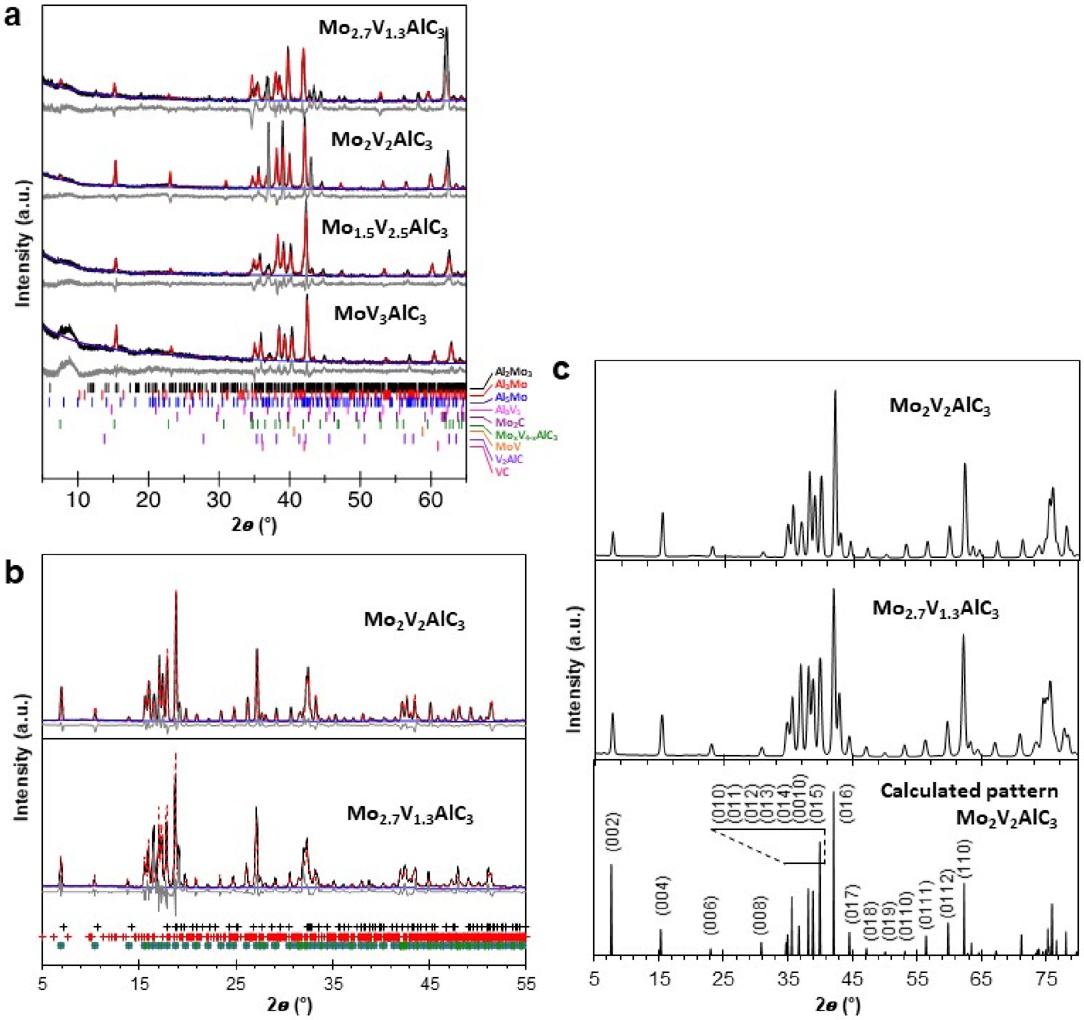

Figure S2. X-Ray diffraction (XRD) patterns of loose MAX powders for Rietveld refinement (RR) and purity determination on GSAS-II code. **a.** Conventional XRD patterns recorded on Rigaku Smartlab (from top to bottom: $Mo_{2.7}V_{1.3}AlC_3$, $Mo_2V_2AlC_3$, $Mo_{1,5}V_{2,5}AlC_3$, and MoV_3AlC_3; RR phase peaking for $Mo_{2.7}V_{1.3}AlC_3$, similar for other phases). Experimental data are the dark line, calculated data are the red line, the background is printed in blue and the difference in grey. Impurities, secondary products and purity level are depicted in Table S1 (Supporting Information). **b.** Complementary synchrotron measurements acquired at a wavelength λ = 0.7 nm (from top to bottom: $Mo_2V_2AlC_3$, $Mo_{2.7}V_{1.3}AlC_3$), and **c.** synchrotron data reported for a conventional Cu Kα radiation (λ = 1.54 nm), through equation $\theta_{K\alpha} = \arcsin\left(\frac{E_\lambda \sin\left(\frac{\theta_\lambda}{2}\right)}{E_{K\alpha}}\right)$, with $E_{K\alpha}$ = 0.8051 keV and E_λ = 1.77 keV. From top to bottom: $Mo_2V_2AlC_3$, $Mo_{2.7}V_{1.3}AlC_3$ and the calculated pattern of $Mo_2V_2AlC_3$.

Table S1. Evaluation of impurities, secondary phases and $Mo_xV_{4-x}AlC_3$ purity level by Rietveld refinement (GSAS-II code, figure S1, Supporting Information)

	Intermetallic (at. %)				Carbide (at. %)			
	Al_5Mo	Al_3Mo	Al_2Mo_3	MoV	VC	V_2AlC	Mo_2C	**$Mo_xV_{4-x}AlC_3$**
$Mo_{2.7}V_{1.3}AlC_3$	3.10	0	3.2	0	0	0	18.42	75.28
$Mo_2V_2AlC_3$	6.30	1.3	0	0	3.20	0	0	89.20
$Mo_{1.5}V_{2.5}AlC_3$	2.74	0.29	0	0.20	0	5.19	0	91.58
MoV_3AlC_3	0	4.26	0	0	0.19	0.19	0.19	95.17

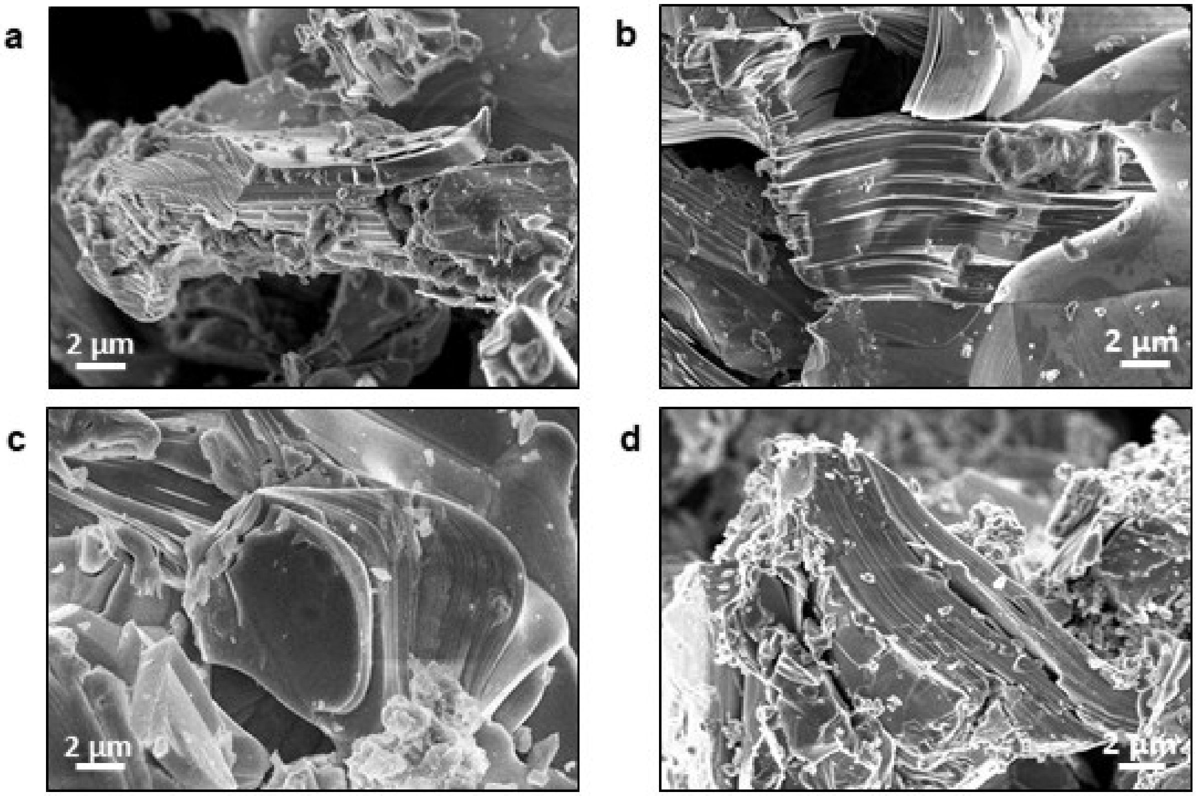

Figure S3. Scanning electron microscopy images of layered $Mo_xV_{4-x}AlC_3$ MAX particles: **a.** $Mo_{2.7}V_{1.3}AlC_3$, **b.** $Mo_2V_2AlC_3$, **c.** $Mo_{1.5}V_{2.5}AlC_3$, **d.** MoV_3AlC_3.

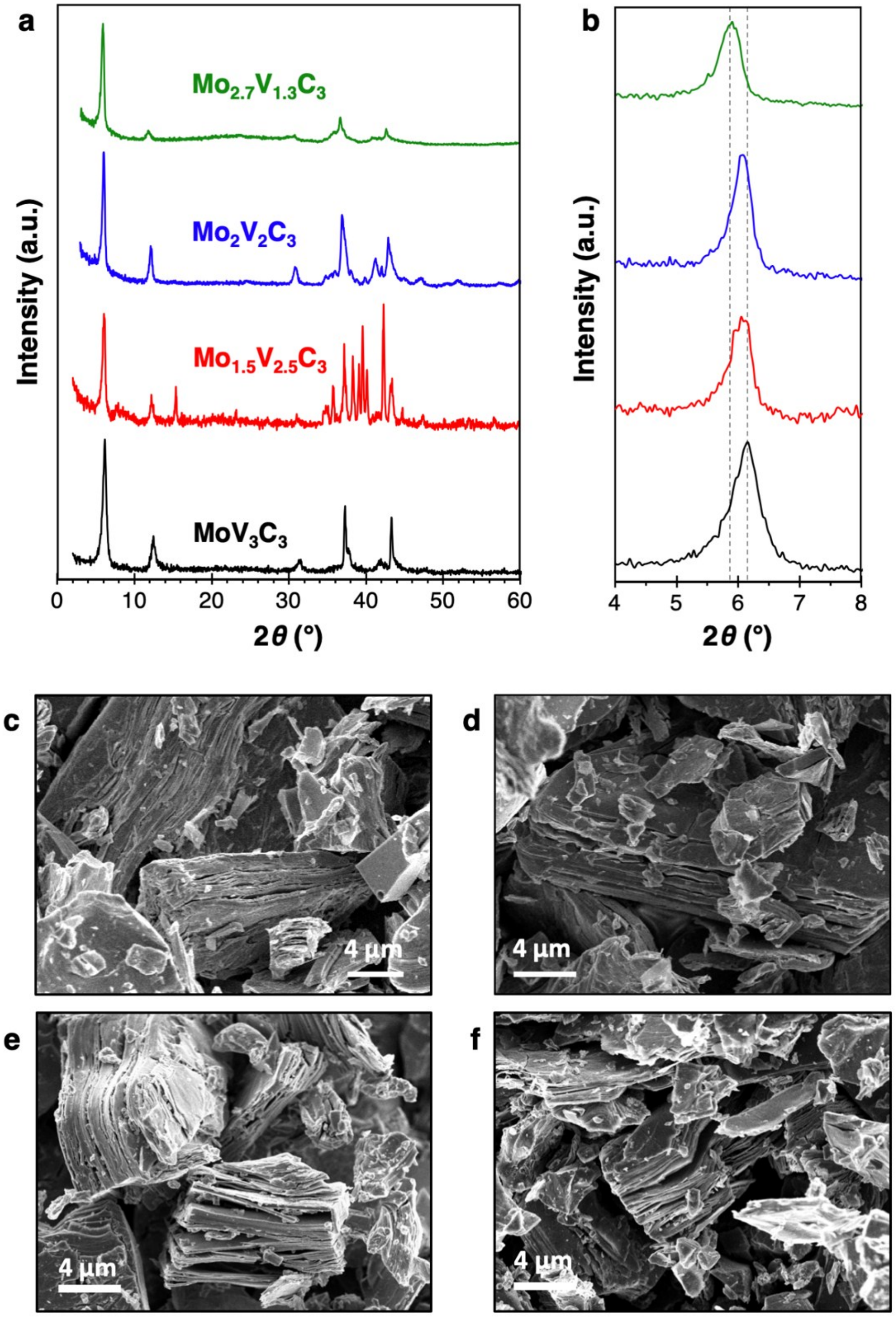

Figure S4. Characterization of multilayer powders after etching in 50% hydrofluoric acid for 96 h at 50 °C. **a.** X-ray diffraction of multilayer MXene powders (from top to bottom: $Mo_{2.7}V_{1.3}C_3$, $Mo_2V_2C_3$, $Mo_{1.5}V_{2.5}C_3$, MoV_3C_3). **b.** Evidence of the (002) peak shift (black arrow) to the highest 2^{θ} from $Mo_{2.7}V_{1.3}C_3$ to MoV_3C_3 multilayers. Scanning electron microscopy images of multilayers MXene: **c.** $Mo_{2.7}V_{1.3}C_3$, **d.** $Mo_2V_2C_3$, **e.** $Mo_{1.5}V_{2.5}C_3$ and **f.** MoV_3C_3 all showing an accordion-like morphology.

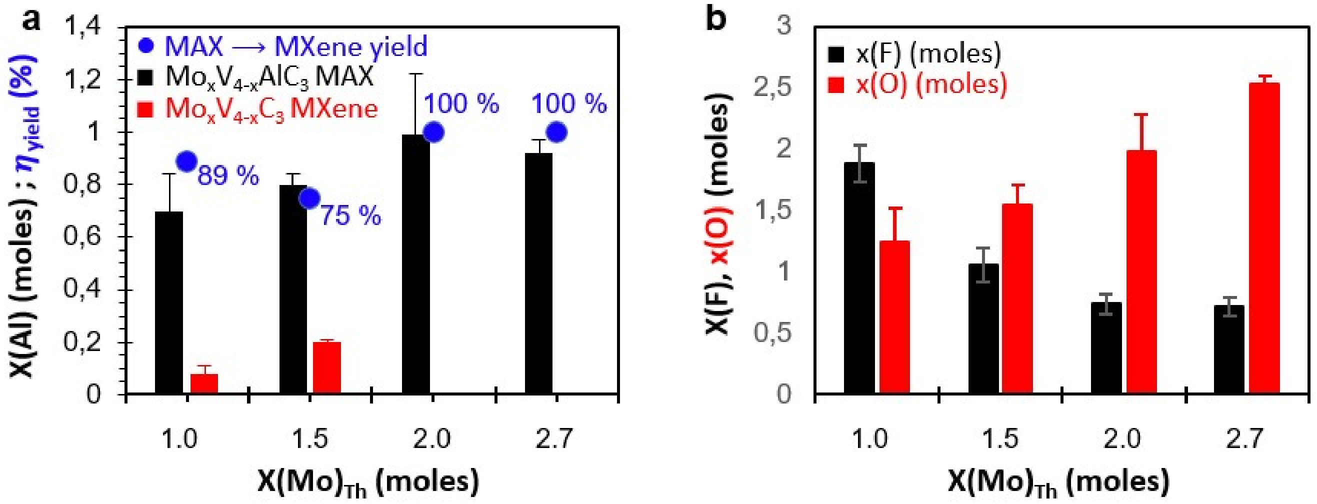

Figure S5. Chemical characterization of $Mo_xV_{4-x}AlC_3$ MAX powders and $Mo_xV_{4-x}C_3$ multilayer MXene produced after etching MAX in 50% hydrofluoric acid at 50 °C for 96 h. **a.** Aluminum content, x(Al) (moles), in the MAX and MXene after etching and, yield of delamination, $\eta = x(Al)_{MXene}/x(Al)_{MAX}$ (%) as a function of the composition $x(Mo)_{Th}$ (moles). **b.** Evaluation of the oxygen and fluorine content (moles) of the MXene MLs as a function of the composition $x(Mo)_{Th}$ (moles). x(Al), x(O) and x(F) are determined by energy dispersive X-ray spectroscopy, focusing on a multilayer MXene and neglecting other particles to exclude any effect of eventual impurities on the results and, the values and errors result from at least 4 measurements on different particles. $x(Mo)_{Th}$ (moles) reflects the expected Mo content in the MXene multilayer *(and MAX)* powders: $x(Mo)_{Th} = 1$, $MoV_3(Al)C_3$; $x(Mo)_{Th} = 1.5$, $Mo_{1.5}V_{2.5}(Al)C_3$; $x(Mo)_{Th} = 2$, $Mo_2V_2(Al)C_3$; $x(Mo)_{Th} = 2.7$, $Mo_{2.7}V_{1.3}(Al)C_3$.

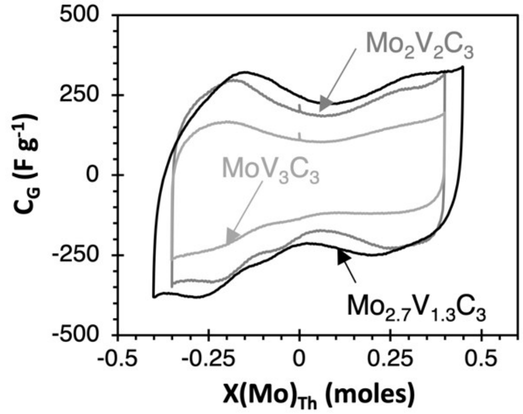

Figure S6. Cyclic voltammetry on films of (from the highest to the lowest gravimetric capacitance, C_G) $Mo_{2.7}V_{1.3}C_3$, $Mo_2V_2C_3$, MoV_3C_3, at 10 mV s^{-1}. Etching conditions: 96 h, 50% hydrofluoric acid, 50 °C.

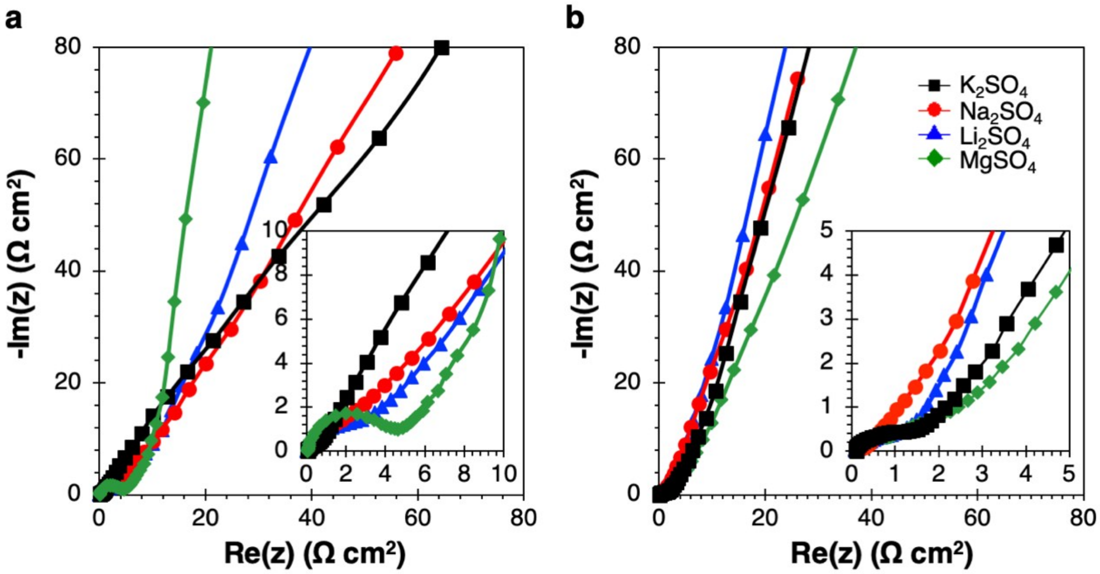

Figure S7. Nyquist plots at 10 mV on $Mo_{2.7}V_{1.3}C_3$ films in various **a.** non-acidified electrolytes pH ∼7 and **b.** acidified electrolytes 2.19 < pH < 2.36 (with H_2SO_4) in half cells.

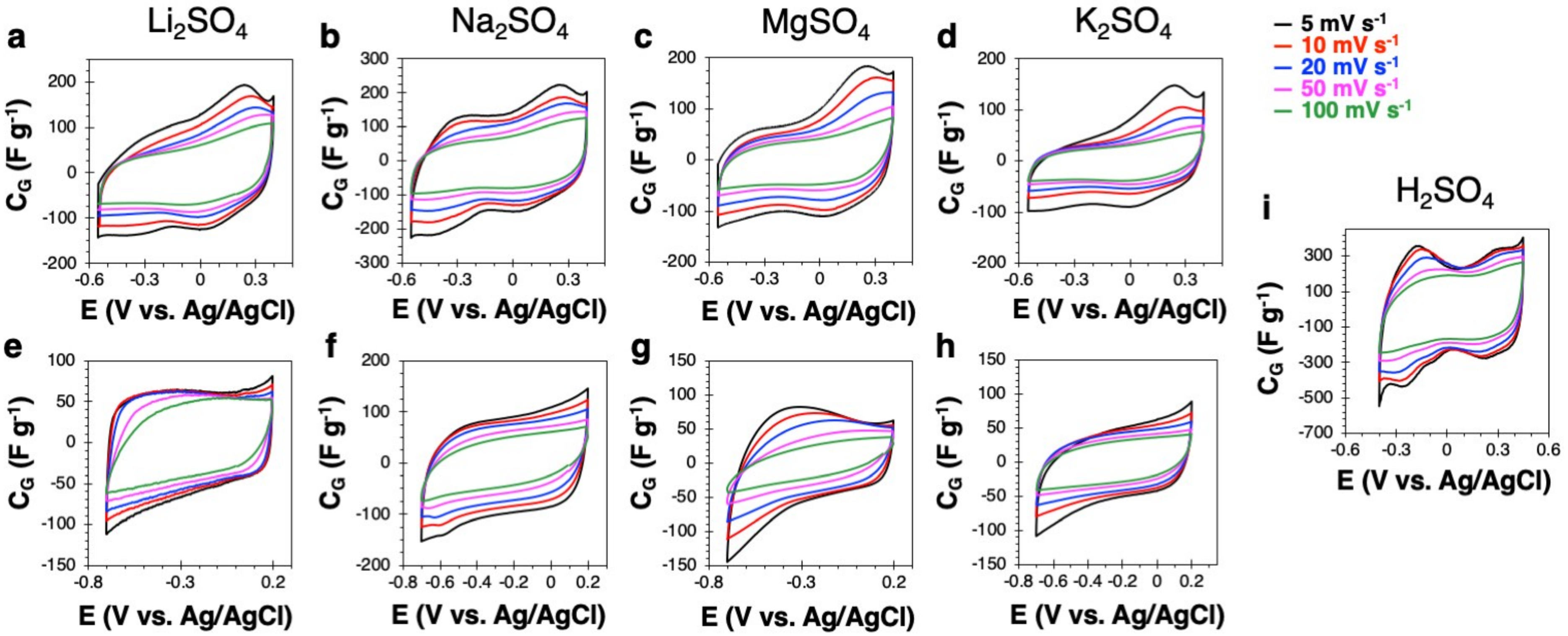

Figure S8. Cyclic voltammograms recorded at scan rates of 5, 10, 20, 50 and 100 mV s^{-1} for acidified **a.** Li_2SO_4, **b.** Na_2SO_4, **c.** $MgSO_4$, **d.** K_2SO_4 electrolytes with H_2SO_4 (2.19 ≤ pH ≤ 2.36), non-acidified **e.** Li_2SO_4, **f.** Na_2SO_4, **g.** $MgSO_4$, **h.** K_2SO_4 electrolytes and, **i.** acidic 1 M H_2SO_4 electrolytes

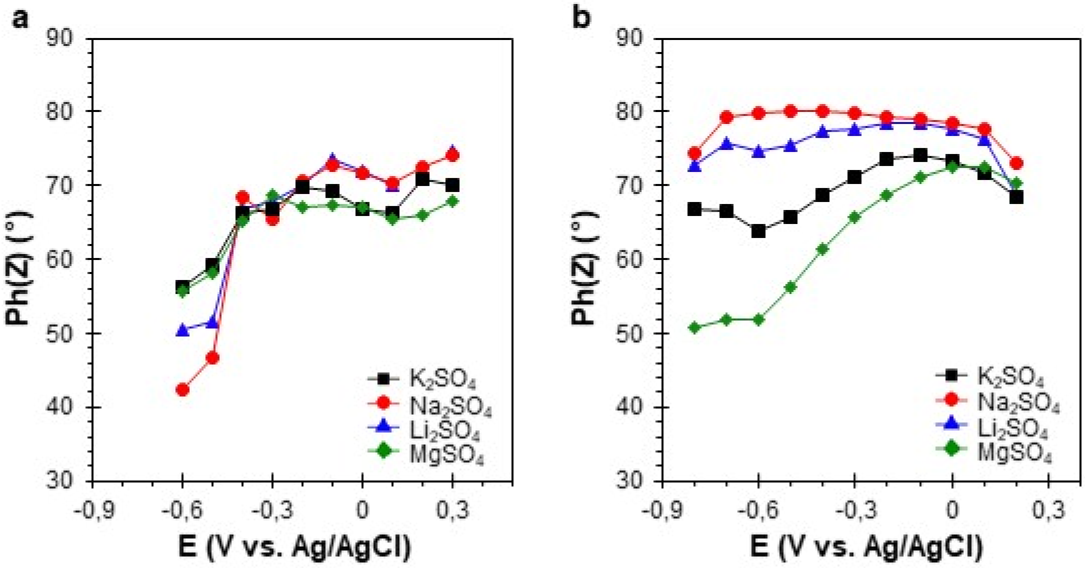

Figure S9. Phase angle at 10 mHz for various applied potential within the electrochemical window (every 100 mV) of MXene in **a.** acidified (2.19 ≤ pH ≤ 2.36) and **b.** non-acidified electrolytes depicting capacitive (90°) to diffusion controlled (45°) activity of $Mo_{2.7}V_{1.3}C_3$ in 1 M Li_2SO_4, 1 M Na_2SO_4, 0.5 M K_2SO_4, 1 M $MgSO_4$.

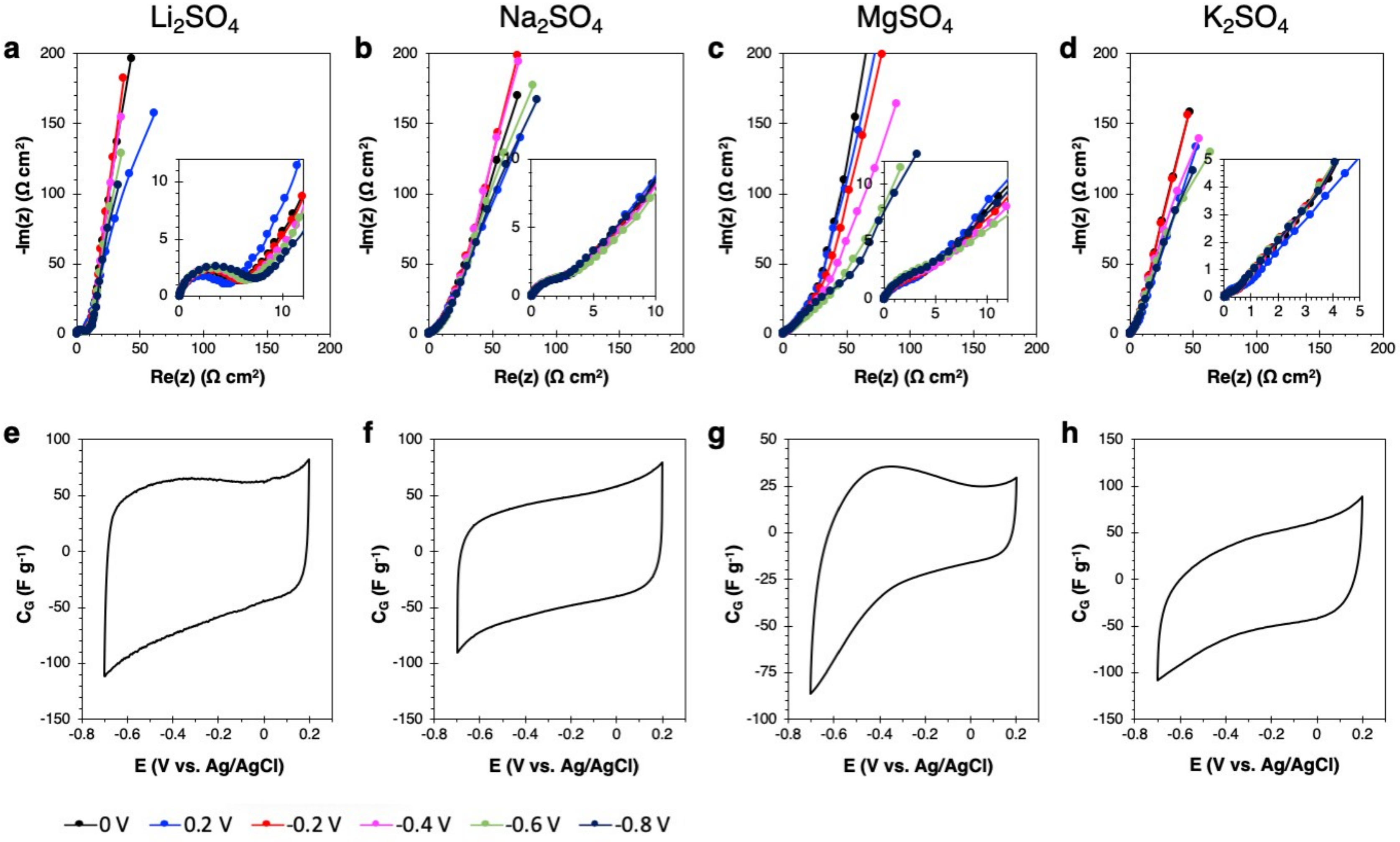

Figure S10. Impedance spectroscopy analysis of $Mo_{2.7}V_{1.3}C_3$ MXene in various non-acidified electrolytes (1 M Li_2SO_4, 1 M Na_2SO_4, 1 M $MgSO_4$, 1 M K_2SO_4) for potential ranging from 0.2 V vs. Ag/AgCl to -0.8 V vs. Ag/AgCl. **a-d.** Nyquist in **a.** Li_2SO_4, **b.** Na_2SO_4, **c.** $MgSO_4$ and **d.** K_2SO_4. **e-h.** Corresponding cyclic voltammograms at 5 mV s^{-1} for **e.** Li_2SO_4, **f.** Na_2SO_4, **g.** $MgSO_4$ and **h.** K_2SO_4.

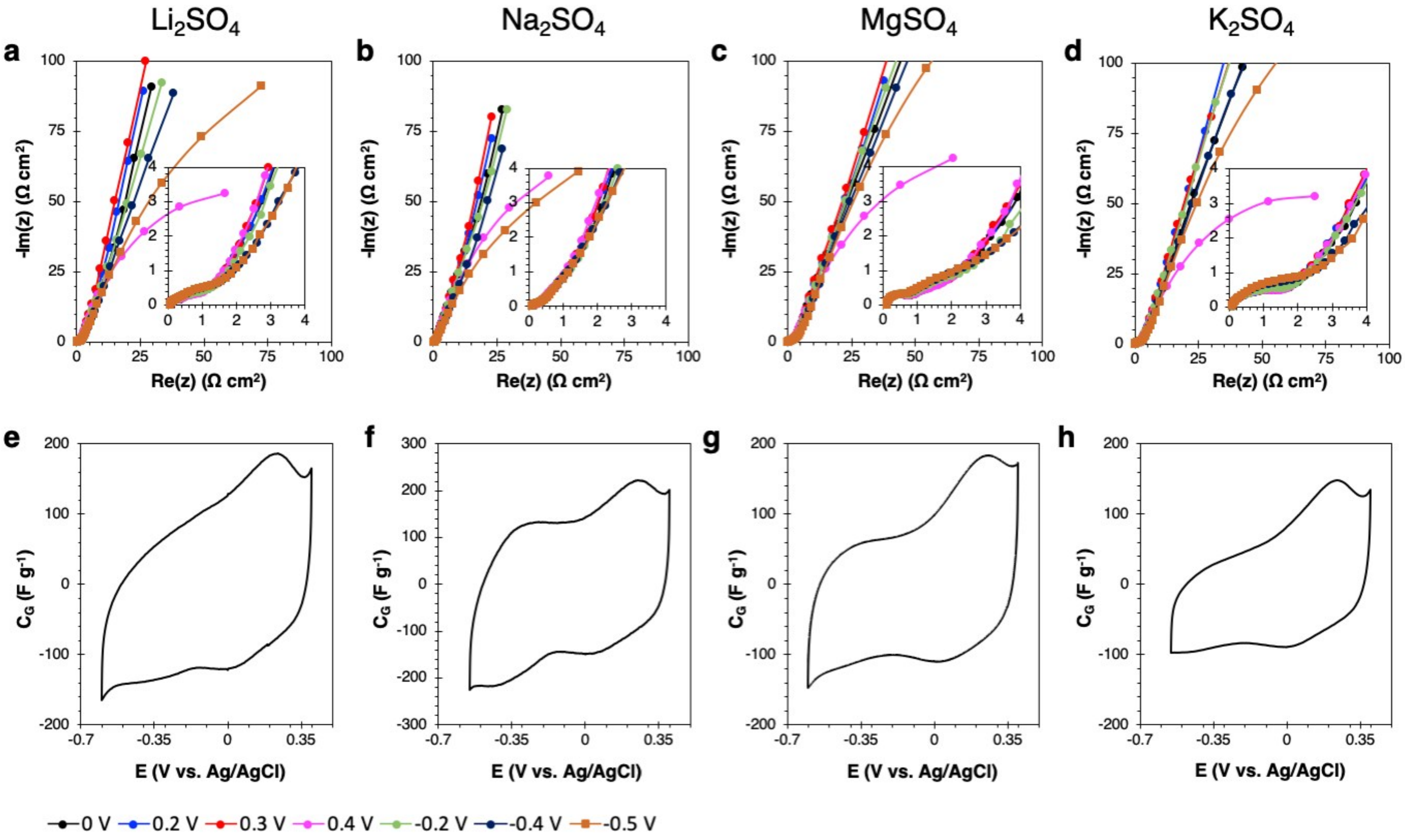

Figure S11. Impedance spectroscopy analysis of $Mo_{2.7}V_{1.3}C_3$ MXene in various acidified electrolytes (1 M Li_2SO_4 pH 2.3, 1 M Na_2SO_4 pH 2.32, 1 M $MgSO_4$ pH 2.19, 1 M K_2SO_4 pH 2.36) for potentials ranging from 0.4 V vs. Ag/AgCl to -0.5 V vs. Ag/AgCl **a-d.** Nyquist in **a.** Li_2SO_4 pH 2.3, **b.** Na_2SO_4 pH 2.32, **c.** $MgSO_4$ pH 2.19 and **d.** K_2SO_4 pH 2.36. **e-h.** Corresponding cyclic voltammograms at 5 mV s^{-1} for **e.** Li_2SO_4 pH 2.3, **f.** Na_2SO_4 pH 2.32, **g.** $MgSO_4$ pH 2.19 and **h.** K_2SO_4 pH 2.36

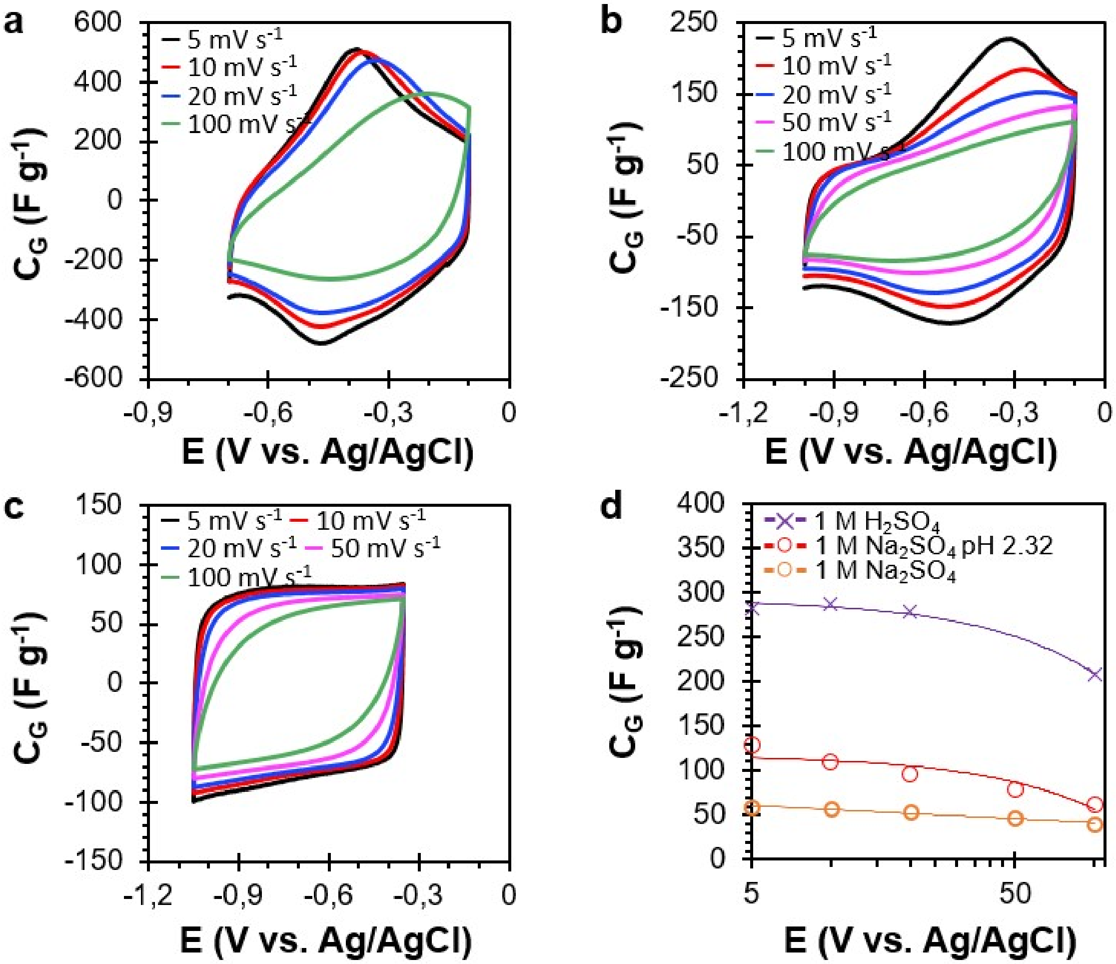

Figure S12. Characterization of Ti_3C_2 electrode within the condition of the asymmetric all-MXene supercapacitor. Cyclic voltammetry of Ti_3C_2 in **a.** H_2SO_4 1 M, **b.** 1 M Na_2SO_4 pH 2.32, **c.** non-acidified 1 M Na_2SO_4, and **d.** gravimetric capacity from 5 to 100 mV s^{-1}.

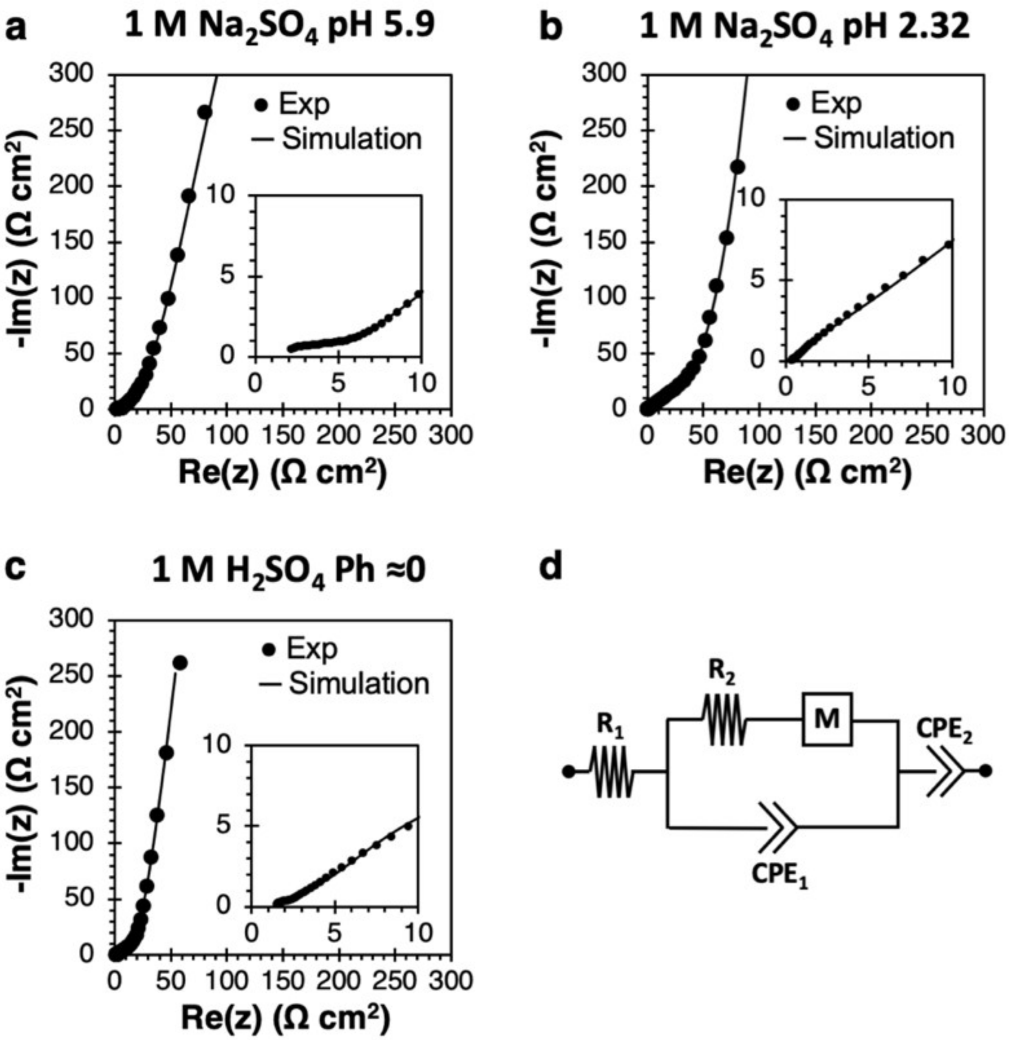

Figure S13. Fitting of experimental data from impedance spectroscopy analysis of all-MXene supercapacitor in **a.** 1 M Na_2SO_4 pH 5.9, **b.** 1 M Na_2SO_4 pH 2.32, **c.** 1 M H_2SO_4 pH ca. 0 (lines are fits and circles are experimental data). **d.** Equivalent electrical circuit.

The equivalent electrical circuit employed for fitting is modified from the literature.[2,3] The impedance response is characteristic of a pseudocapacitor system.[4,5] R_1 is the electrode series resistance (ESR), which mainly reflects the quality of the contact between the active material and the collector, as well as the overall resistance of this contact. Fitted Nyquist plots show that the double layer capacitance can be substituted by a CPE in order to fit the non-ideal high frequency semi-circle (depressed aspect of semi-circle). Finally, R_2 stands for the charge transfer resistance and M represent the restricted linear diffusion across the electrode-electrolyte interface. ESR of each system evolves from 0.3 to 2 Ω cm² which accounts for a good collector to MXene contact with low resistance.

1. M. Alhabeb, K. Maleski, B. Anasori, P. Lelyukh, L. Clark, S. Sin and Y. Gogotsi, *Chem. Mater.*, 2017, **29**, 11.
2. H. Gao, X. Wang, G. Wang, C. Hao, S. Zhoua and C. Huang, *Nanoscal*e, 2018, **10**, 10190-10202.
3. H. Gao, X. Wang, G. Wang, C. Hao, C. Huang and C. Jiang, *J. Mater. Chem. C*, 2019, **7**, 13267-13278
4. Q. Jiang, N. Kurra, M. Alhabeb, Y. Gogotsi, H.N. Alshareef, *Adv. Energy Mater*., 2018, **8**, 1703043.
5. H. Avireddy, B.W. Byles, D. Pinto, J.M.D. Galindo, J.J. Biendicho, X. Wang, C. Flox, O. Crosnier, T. Brousse, E. Pomerantseva, J.R. Morante, Y. Gogotsi, *Nano Ener*gy, 2019, **64**, 103961.